Continuous-Phase Modulation Waveform Simulation

Bruce E. Wahlen, Sidney J. Graser,
Calvin Y. Mai, and Tracey A. Burr
Space and Naval Warfare Systems Center
San Diego, CA 92152

March 14, 2000

1 Introduction

The Space and Naval Warfare Systems Center, San Diego (SPAWARSYSCEN-SD) and the Defense Information Systems Agency (DISA) Joint Interoperability and Engineering Organization (JIEO) have been investigating methods to increase data throughput rates to 12 kilobits per second (kbps) and 64 kbps over the 5- and 25-kHz UHF SATCOM channels, respectively. There are, however, many challenges to bandwidth efficient communication over the UHF SATCOM channel. For example, the hard-limiting transponder on DoD UHF satellites and the non-linear amplifiers often used in earth station and satellite high power amplifiers have the effect of removing all amplitude modulation from the transmitted signal and producing spectral re-growth.

In view of these challenges two well-known bandwidth efficient techniques, trellis-coded modulation (TCM) and continuous-phase modulation (CPM), were originally considered as methods to increase the UHF SATCOM data rates. After a period of testing both methods, CPM was proposed as the new 5- and 25-kHz UHF SATCOM standard waveform in MIL-STD-188-181B [1].

The purpose of this paper is to provide a detailed description of uncoded and coded CPM, including proofs of some of its properties, some examples, discussion of performance trade-offs, derivation of the baseband correlation receiver, review of synchronization methods, and performance simulations of some of the CPM waveforms specified in MIL-STD-188-181B [1]. The remainder of this document provides a description of the CPM waveform (section 2), the coded CPM waveform (section 3), synchronization methods (section 4), and simulation results (section 5). To obtain a copy of the simulation software written in MATLAB code please contact the third author (email: cmai@spawar.navy.mil).

2 CPM Waveform

CPM is a constant amplitude, phase-modulated technique in which the phase is constrained to be continuous everywhere, in particular at symbol transitions; see Anderson, Aulin and Sundberg [2] for a detailed description of this modulation technique. This scheme of smoothing out the phase discontinuities at symbol transitions reduces spectral spreading relative to other constant amplitude techniques which have phase discontinuities at symbol transitions. For example, at symbol transitions quaternary phase-shift keying (QPSK) can change phase by $\pm 90\,^\circ$ or $180\,^\circ$ and offset QPSK (OQPSK) can change phase by $\pm 90\,^\circ$. CPM modulation includes both continuous-phase frequency-shift keying (CPFSK) and minimum-shift keying (MSK) as special cases.

2.1 Waveform Definition

The CPM waveform is defined by

$$s(t, \boldsymbol{\alpha}) \triangleq \sqrt{\frac{2E_s}{T_s}} \cos(2\pi f_0 t + \phi(t, \boldsymbol{\alpha})), \tag{1}$$

where E_s is the *energy per symbol*, T_s is the *symbol duration* and f_0 is the *carrier frequency*. After application of a familiar trigonometric identity, the CPM waveform may be represented equivalently as

$$s(t, \boldsymbol{\alpha}) = \sqrt{\frac{2E_s}{T_s}} \left[I(t, \boldsymbol{\alpha}) \cos 2\pi f_0 t - Q(t, \boldsymbol{\alpha}) \sin 2\pi f_0 t \right], \tag{2}$$

where the *in-phase* component, $I(t, \boldsymbol{\alpha})$, is defined as

$$I(t, \boldsymbol{\alpha}) \triangleq \cos \phi(t, \boldsymbol{\alpha}) \tag{3}$$

and the *quadrature* component, $Q(t, \boldsymbol{\alpha})$, is defined as

$$Q(t, \boldsymbol{\alpha}) \triangleq \sin \phi(t, \boldsymbol{\alpha}). \tag{4}$$

In this technique, the transmitted information is carried in the *phase*, $\phi(t, \boldsymbol{\alpha})$, defined by the expression

$$\phi(t, \boldsymbol{\alpha}) = 2\pi \sum_{i=-\infty}^{+\infty} h_{\underline{i}} \alpha_i q(t - iT_s), \tag{5}$$

in which the *data sequence*, $\boldsymbol{\alpha} = (\dots, \alpha_{-1}, \alpha_0, \alpha_{+1}, \dots)$, is convolved with a *phase response* function, $q(t)$. Each *data symbol*, α_i, is generated by first grouping an incoming *stream of bits*, $b_{i'}$, into successive *blocks of information bits*, $\boldsymbol{b}_i$, of length m, and then mapping each block of information bits into an M-ary symbol alphabet $\mathcal{M} = \{\pm 1, \pm 3, \dots, \pm(M-1)\}$, where $M = 2^m$. It follows, then, that $T_s = mT_b$, where T_b is the *bit duration*, and also that the *symbol rate*,

2

$R_s \triangleq 1/T_s$, is given by $R_s = R_b/m$, where R_b is the *bit rate*. See below for a block diagram of a baseband CPM transmitter (Fig. 1).
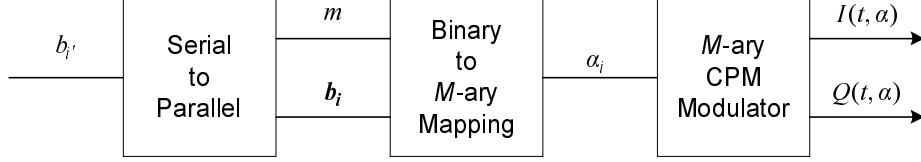

Figure 1: Block diagram of baseband CPM transmitter.

The sequence of real-valued constants, $\mathcal{H} = \{h_{\underline{i}} : \underline{i} = i \bmod H\}$, called *modulation indices*, determines how much the phase changes with each data symbol. The meaning of the notation, $h_{\underline{i}}$, in equation (5) is that only H different constants are used in a cyclical fashion, *i.e.*, $\ldots, h_0, h_1, \ldots, h_{H-1}, h_0, h_1, \ldots, h_{H-1},$ $\ldots$. When $H = 1$, there is only one modulation index, denoted $h_0 = h$, and the waveform is called *constant-h* CPM or simply CPM; when $H > 1$, the waveform is called *multi-h* CPM (MHCPM).

The phase response, $q(t)$, describes how the underlying phase change, $2\pi\alpha_i h_{\underline{i}}$, evolves with time and is defined as the integral of the *instantaneous frequency pulse*, $g(t)$, by the equation

$$q(t) \triangleq \int_{-\infty}^{t} g(\tau) \, d\tau. \tag{6}$$

From this integral equation and equation (5) it is clear that the shape of $g(t)$ determines the smoothness of the information carrying phase, $\phi(t, \boldsymbol{\alpha})$. In particular, the greater the smoothness of $g(t)$ the more gradual are the phase transitions, producing a faster rate of reduction of the spectral side lobes of the waveform.

It is assumed that the pulse, $g(t)$, is *bounded*, *i.e.*, $|g(t)| \leq B < +\infty$ for all t, and of *finite duration*, LT_s, *i.e.*, $g(t) \equiv 0$ for $t < 0$, and $t > LT_s$. Systems for which $L = 1$ allow pulse shaping only over a single symbol interval and are called *full-response* [3]; systems for which $L > 1$ allow pulse shaping over several symbol intervals and are called *partial-response* [4]. See below (Fig. 2) for some examples of full-response and partial-response pulses of different shapes and their phase responses. The pulse specified by MIL-STD-188-181B is the full-response rectangular shape referred to as the 1REC pulse (Fig. 2, 1REC); constant-h CPM with a 1REC pulse is equivalent to CPFSK.

By virtue of the smoothing provided by the operation of integration and after normalizing $g(t)$ if necessary, it can be proved that the phase response satisfies the following properties:

1. $q(t)$ is a continuous function, for $-\infty \leq t \leq +\infty$, and

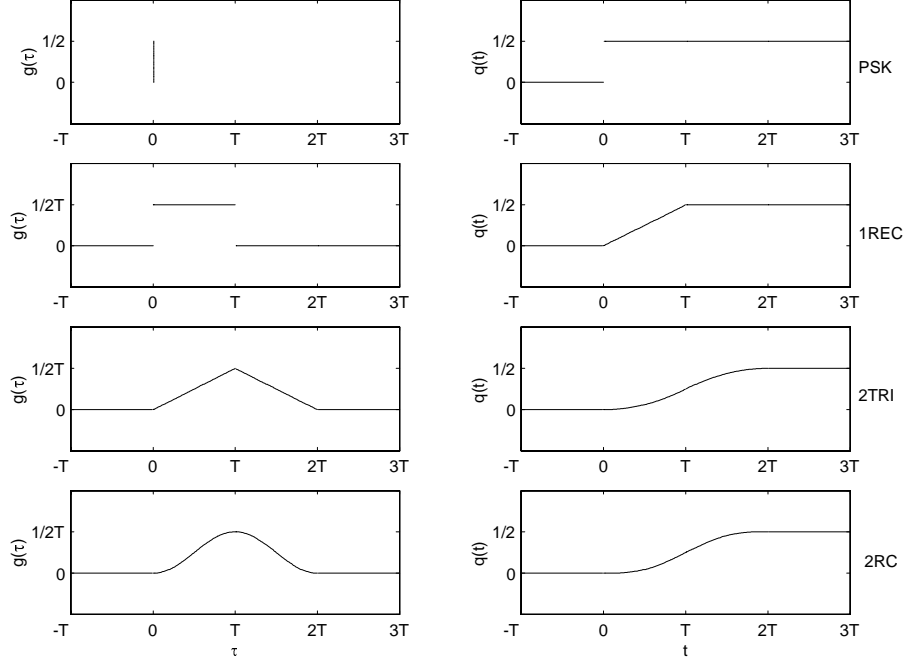2. $q(t) = \begin{cases} 0, & \text{if } t \leq 0 \\ \frac{1}{2}, & \text{if } t \geq LT_s. \end{cases}$

3

Figure 2: Instantaneous frequency pulses, $g(\tau)$, and their corresponding phase responses, $q(t)$, for phase shift keying (PSK), full-response rectangular (1REC), partial-response ($L = 2$) triangular (2TRI), and partial-response ($L = 2$) raised cosine (2RC).

Partitioning the sum in equation (5) into three sums over the intervals $-\infty \leq i \leq n-L$, $n-(L-1) \leq i \leq n$ and $n+1 \leq i \leq +\infty$, and then applying property 2 above to $q(t - iT_s)$ in each sum, it follows that during the nth *symbol interval*, defined by $nT_s \leq t < (n+1)T_s$, the phase can be expressed as

$$\phi(t, \boldsymbol{\alpha}) = \theta(t, \boldsymbol{\alpha}) + \theta_n, \qquad (7)$$

where

$$\theta(t, \boldsymbol{\alpha}) \triangleq 2\pi \sum_{i=n-(L-1)}^{n} h_{\underline{i}}\alpha_i q(t - iT_s) \qquad (8)$$

and

$$
\begin{aligned}
\theta_n &\triangleq \pi \sum_{i=-\infty}^{n-L} h_{\underline{i}}\alpha_i \\
&= \theta_{n-1} + \pi h_{\underline{n-L}}\alpha_{n-L}.
\end{aligned} \qquad (9)
$$

4

To prove continuity of the phase at symbol transitions as claimed above for CPM waveforms, we let t_{n_k} be a sequence of points belonging to the nth symbol interval for which $\lim_{k\to\infty} t_{n_k} = (n+1)T_s$. Applying properties 1 and 2 above, it can be shown that

$$
\begin{aligned}
\lim_{k\to\infty} \phi(t_{n_k}, \boldsymbol{\alpha}) &= \theta((n+1)T_s, \boldsymbol{\alpha}) + [\theta_n + \pi h_{\underline{n+1-L}}\alpha_{n+1-L}] \\
&= \phi((n+1)T_s, \boldsymbol{\alpha}), \quad\quad\quad (10)
\end{aligned}
$$

by equations (9) and (7). This proves continuity of the phase at symbol transitions, and it shows that $\pi h_{\underline{n-L}}\alpha_{n-L}$ in equation (9) functions as a *continuity correction* term at symbol transitions.

2.2 Performance Trade-Offs

Choice of g and of the values of the system parameters $M, H, \{h_{\underline{i}}\}$, and L for a particular application of CPM or MHCPM is, as in the case of other waveforms, determined by a consideration of trade-offs among various indicators of system performance. Performance indicators included are signal energy or power, complexity, bit error rate (BER), and spectral efficiency, measured by the width of the main and side spectral lobes, the rate of reduction of the spectral side lobes, or the fractional out-of-band power. For example, increasing M, H, or L can improve performance with respect to BER and required signal energy (Anderson *et al.* [2]), but such increases also degrade performance in terms of increased complexity, especially receiver complexity (Sasase and Mori [5]). Other trade-offs are described below, first for the case $H = 1$ and then for $H > 1$.

$H = 1$: In this case Anderson *et al.* [2] state that if $g(\tau)$ has c continuous derivatives, or equivalently that $q(t)$ has $c + 1$ continuous derivatives, then for any values of M, h, or L the power spectral density (PSD), $S(f)$, decreases asymptotically as

$$ S(f) \sim |f|^{-(2c+6)} \quad (f \to \infty). $$

From this asymptotic relationship, it follows that the PSD of all PSK modulation schemes decays like $|f|^{-2}$, the PSD of all CPM schemes with rectangular pulse decays like $|f|^{-4}$, the PSD of all CPM schemes with triangular pulse like $|f|^{-6}$, and the PSD of all CPM schemes with raised cosine pulse like $|f|^{-8}$. However, since the asymptotic decay rate of the PSD may occur very far from the center frequency, increasing c is not the most effective means of achieving spectrally efficient modulation; in fact, Anderson *et al.* [2] point out that for fixed L large values of c produce large main and first side spectral lobes. Sasase and Mori [5] also state that the width of the main spectral lobe decreases with increasing L but increases with increasing h or M. Finally, Anderson and Sundberg [6] note that larger values of h generally lead to better BER performance but a wider spectrum.

$H > 1$: Increasing H potentially decreases BER for fixed values of E_b/N_0 or decreases required E_b/N_0 for fixed values of BER, but this trade-off between

BER or required E_b/N_0 and increased complexity is unfavorable beyond $H = 4$. Sasase and Mori [5] and others report that 4-ary 2-h MHCPM achieves signal energy improvement of about 2 dB over both 4-ary single-h and binary MHCPM at the same bandwidth. Letting $\overline{h} = (1/H) \sum_{i=0}^{H-1} h_i$ denote the *mean modulation index*, Anderson *et al.* [2, Table 3.1] present results that suggest that most good schemes with $H = 2, 3$, or 4 should have values of $\overline{h}$ between 0.5 and 0.7 with the values of h_i close together. They also report that the spectral characteristics of a MHCPM scheme with mean modulation index $\overline{h}$ and where the values of h_i are close together is similar to a CPM scheme with $h = \overline{h}$.

2.3   State Model

Defining the *state vector*, $\boldsymbol{\sigma}_n \in \Sigma$, by

$$\boldsymbol{\sigma}_n \triangleq (\theta_n, \alpha_{n-1}, \alpha_{n-2}, \dots, \alpha_{n-(L-1)}), \tag{11}$$

it is clear from equations (7) and (8) that the phase and, hence the signal, is completely determined over the interval $[nT_s, (n+1)T_s]$ and subsequent intervals by $\boldsymbol{\sigma}_n$ and new data symbols $\alpha_n, \alpha_{n+1}, \dots$. We note that the *memory* introduced into the phase process by the continuity constraint and pulse length, L, is reflected in the dependence of the state vector on the *phase state*, θ_n, and the $L-1$ previous data symbols, $\alpha_{n-1}, \alpha_{n-2}, \dots, \alpha_{n-(L-1)}$. CPM systems that are practical in a decoding sense must be representable by a finite number of states with an associated *state trellis*.

The finite-state requirement for practical decoding can be fulfilled only if θ_n takes on a finite number of values. This constraint on θ_n is satisfied under the conditions that: (1) for each $i = 0, 1, \dots, H-1$ the modulation index, h_i, is a rational number expressible as $h_i = 2r_i/p$, where r_i and p are integers, and (2) the $\gcd(r_0, r_1, \dots, r_{H-1}, p) = 1$, where gcd denotes the *greatest common divisor*. Substituting expressions for h_i in the form given by condition (1) into the first line of equation (9) it follows that

$$\theta_n = (2\pi/p) \sum_{i=-\infty}^{n-L} r_i \alpha_i.$$

Then, applying the Euclidean algorithm to the summation, it can be seen that the phase states are given by

$$\theta_n \in \Theta = \left\{ S_j : S_j = j\frac{2\pi}{p}, \text{ for } j = 0, 1, \dots, p-1 \right\} \pmod{2\pi}. \tag{12}$$

Letting the operator $|\cdot|$ denote the cardinality of a set, it is clear that $|\Theta| = p$ and, therefore, that as required for practical decoding, $|\Sigma|$ is finite and furthermore from equation (11) that

$$|\Sigma| = pM^{(L-1)}. \tag{13}$$

6

Condition (2) insures that $|\Theta|$ is minimal in size since if $\gcd(r_{\underline{0}}, r_{\underline{1}}, \dots, r_{\underline{H-1}}, p) = d > 1$ and $p = \widetilde{p}d$, then by a similar derivation it can be shown that

$$\theta_n \in \widetilde{\Theta} = \left\{ S_j : S_j = j\frac{2\pi}{\widetilde{p}}, \text{ for } j = 0, 1, \dots, \widetilde{p} - 1 \right\} \pmod{2\pi},$$

in which case $|\widetilde{\Theta}| = \widetilde{p} < p$ and $|\widetilde{\Sigma}| = \widetilde{p}M^{(L-1)}$.

If any of the modulation indices is given by $h_{\underline{i}} = r_{\underline{i}}/p$ with $r_{\underline{i}}$ an *odd* number, first express $h_{\underline{i}}$ equivalently as $h_{\underline{i}} = 2r_{\underline{i}}/p'$ where $p' = 2p$, and then use p' in place of p in equations (12) and (13) to compute the values of the phase states, S_j, and the number of states, $|\Sigma|$, respectively. For notational purposes, we note that Θ can be partitioned as $\Theta = \Theta_{\text{even}} \cup \Theta_{\text{odd}}$, where

$$\Theta_{\text{even}} \triangleq \{ S_j \in \Theta : j \text{ is even} \}$$

is the subset of states with *even-numbered* indices and

$$\Theta_{\text{odd}} \triangleq \{ S_j \in \Theta : j \text{ is odd} \}$$

is the subset of states with *odd-numbered* indices.

Remark 1 *If $H = 1$ and p is even it can be shown from equation (9) that if $\theta_n \in \Theta_{even}$ then $\theta_{n+1} \in \Theta_{odd}$ and if $\theta_n \in \Theta_{odd}$ then $\theta_{n+1} \in \Theta_{even}$. Thus, if p is even, the number of phase states occupied in any symbol interval is reduced by half.*

2.4 Full-Response CPM

In the full-response case ($L = 1$) the dependence on $\boldsymbol{\alpha}$ in equation (8) and, hence, in equation (7) involves only the single data symbol α_n, so in this case we adopt the notation $\theta(t, \alpha_n)$ for $\theta(t, \boldsymbol{\alpha})$ and $\phi(t, \alpha_n)$ for $\phi(t, \boldsymbol{\alpha})$. Using this notation in equations (7), (8), and (9), it follows that on the interval $nT_s \leq t < (n+1)T_s$, the phase may be written as

$$\phi(t, \alpha_n) = \theta(t, \alpha_n) + \theta_n, \tag{14}$$

and furthermore that $\theta(t, \alpha_n)$ simplifies to

$$\theta(t, \alpha_n) = 2\pi h_{\underline{n}} \alpha_n q(t - nT_s), \tag{15}$$

and that

$$\theta_n = \theta_{n-1} + \pi h_{\underline{n-1}} \alpha_{n-1}. \tag{16}$$

In this case the state vector, $\boldsymbol{\sigma}_n$, reduces to a scalar given by the phase state, θ_n; the current data symbol, α_n, determines the transition from the current phase state, θ_n, to the next phase state, θ_{n+1}; and this transition defines the actual function of time that is transmitted during the nth symbol interval. For the remainder of this document, we consider only the full-response case with finite-length data sequence $\boldsymbol{\alpha} = (\alpha_0, \alpha_1, \dots, \alpha_I)$.

7

	θ_{n+1}	
θ_n	$\alpha_n = -1$	$\alpha_n = +1$
S_3	S_2	S_0
S_2	S_1	S_3
S_1	S_0	S_2
S_0	S_3	S_1

Table 1: Phase state transitions for MSK.

Example 1 *Consider minimum-shift keying (MSK), which is a special case of binary CPM with a full-response, rectangular pulse (1REC) and a single modulation index, $h = \frac{1}{2} = \frac{2 \cdot 1}{4}$. In this example, $\mathcal{M} = \{-1, +1\}$ and $\boldsymbol{\sigma}_n = \theta_n \in \Theta = \{0, \frac{\pi}{2}, \pi, \frac{3\pi}{2}\}$, where phase state transitions from θ_n to θ_{n+1} are determined according to equation (16). See below (Fig. 3) for a diagram of the phase state trellis for MSK. The effect of an even value of p is seen in that even-numbered (odd-numbered) phase states transition to odd-numbered (even-numbered) phase states as noted above (Remark 1). For encoding (section 2.6.1) and decoding (section 2.6.3), the transition information can be stored in tabular form as above (Table 1). In actual implementation the decoding process can be simplified further using the knowledge that only half of the phase states are occupied at any time.*
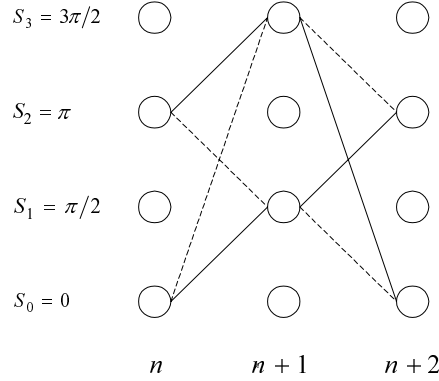

Figure 3: Phase state trellis section for MSK between symbol intervals n and $n + 2$, where transitions generated by $\alpha_n = -1$ and $\alpha_{n+1} = -1$ are depicted with *dashed* lines and transitions generated by $\alpha_n = +1$ and $\alpha_{n+1} = +1$ are depicted with *solid* lines.

For non-binary MHCPM, Table 1 can be expanded easily to allow for dependence on more than two data symbol values and on more than one modulation index. As in the constant-h case (Example 1) there are special cases of MHCPM in which only some of the phase states are occupied at any time, allowing for a

similar simplification of the MHCPM decoding process. See below (Example 2) for a description of such a case.

Example 2 *Consider the 4-ary, 2-h, full-response waveform described in MIL-STD-188-181B [1] where one of the numerators of h_0 and h_1 is an even number and the other is an odd number. From equation (16) it follows that if the value of h_n has an even numerator then an even-numbered (odd-numbered) phase state, θ_n, will transition to an even-numbered (odd-numbered) phase state, θ_{n+1}, and if the value of h_n has an odd numerator then an even-numbered (odd-numbered) phase state, θ_n, will transition to an odd-numbered (even-numbered) phase state, θ_{n+1}. Letting h_n^e denote the case when the value of h_n has an even numerator and h_n^o denote the case when the value of h_n has an odd numerator, these transitions over four symbol intervals can be summarized by the following cyclically repeating diagram*

$$\Theta_{even} \xrightarrow{h_n^e} \Theta_{even} \xrightarrow{h_{n+1}^o} \Theta_{odd} \xrightarrow{h_{n+2}^e} \Theta_{odd} \xrightarrow{h_{n+3}^o} \Theta_{even}.$$

2.5 Baseband Correlation Receiver

Following the derivation in Anderson *et al.* [2], it is assumed that the *received signal*, $r(t)$, is expressible as

$$r(t) = s(t, \boldsymbol{\alpha}) + N(t), \tag{17}$$

where $N(t)$ is *bandpass white Gaussian noise* (BPWGN) given by

$$N(t) = I_N(t) \cos 2\pi f_0 t - Q_N(t) \sin 2\pi f_0 t. \tag{18}$$

The *maximum likelihood sequence estimate* (MLSE) maximizes the *log likelihood function*

$$\log(P(r(t)|\boldsymbol{\alpha}) \approx -\int_{-\infty}^{+\infty} [r(t) - s(t, \boldsymbol{\alpha})]^2 \, dt \tag{19}$$

with respect to the sequence $\boldsymbol{\alpha}$. It is equivalent to maximize the correlation

$$J(\boldsymbol{\alpha}) = \int_{-\infty}^{+\infty} r(t) s(t, \boldsymbol{\alpha}) \, dt \tag{20}$$

with respect to the sequence $\boldsymbol{\alpha}$ as the basis for a correlation receiver. Calculation of this correlation is not feasible in practice, so consider instead

$$J_n(\boldsymbol{\alpha}) = \int_{-\infty}^{(n+1)T_s} r(t) s(t, \boldsymbol{\alpha}) \, dt, \tag{21}$$

which is calculated recursively as

$$J_n(\boldsymbol{\alpha}) = J_{n-1}(\boldsymbol{\alpha}) + Z_n(\boldsymbol{\alpha}, \theta_n), \tag{22}$$

9

where

$$Z_n(\boldsymbol{\alpha}, \theta_n) \triangleq 2 \int_{nT_s}^{(n+1)T_s} r(t) s(t, \boldsymbol{\alpha}) \, dt. \tag{23}$$

The metrics $Z_n(\boldsymbol{\alpha}, \theta_n)$ are seen to be the correlation between the received signal and *all possible* transmitted signal alternatives over the nth symbol interval. To choose the sequence $\widehat{\boldsymbol{\alpha}}$ that maximizes the log likelihood function (19) up to the nth symbol interval we use the well-known Viterbi algorithm (section 2.6.3).

Since we assume full-response CPM we will denote dependence on $\boldsymbol{\alpha}$ in any following equations as a dependence only on α_n as in the previous section. Substituting for $r(t)$ using equation (17) and then substituting for $s(t, \boldsymbol{\alpha})$ and $N(t)$ using equations (2) and (18), respectively, multiplying terms, applying trigonometric identities, and omitting double frequency terms, it can be shown that

$$Z_n(\alpha_n, \theta_n) = \sqrt{2E_s/T_s} \int_{nT_s}^{(n+1)T_s} \left[\widetilde{I}(t, \alpha_n) I(t, \alpha_n) + \widetilde{Q}(t, \alpha_n) Q(t, \alpha_n) \right] dt, \tag{24}$$

where

$$\widetilde{I}(t, \alpha_n) = \sqrt{2E_s/T_s} I(t, \alpha_n) + I_N(t) \tag{25}$$

and

$$\widetilde{Q}(t, \alpha_n) = \sqrt{2E_s/T_s} Q(t, \alpha_n) + Q_N(t). \tag{26}$$

For simplicity, therefore, we consider only the *baseband correlation receiver* defined by equation (24) and shown in block diagram form below (Fig. 4).
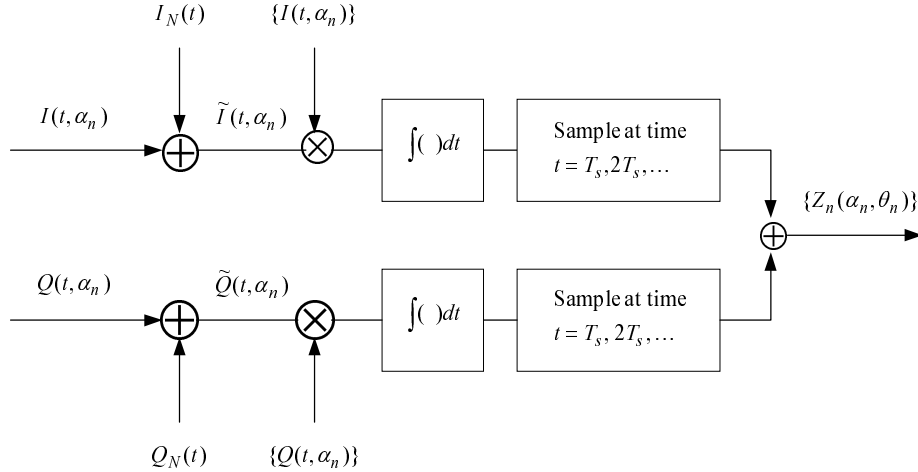

Figure 4: Block diagram of baseband CPM receiver.

From equations (25) and (26) and as shown in the above receiver structure, the *received* in-phase signal, $\widetilde{I}(t, \alpha_n)$, is the sum of the *transmitted* in-phase signal, $I(t, \alpha_n)$, and the in-phase component, $I_N(t)$, of the BPWGN; while the *received* quadrature signal, $\widetilde{Q}(t, \alpha_n)$, is the sum of the *transmitted* quadrature signal, $Q(t, \alpha_n)$, and the quadrature component, $Q_N(t)$, of the BPWGN. For clarification of equation (24) and of the receiver diagram (Fig. 4), we emphasize that the baseband receiver correlates the received in-phase signal over one symbol interval with *all possible* transmitted in-phase alternatives over that symbol interval, namely $\{I(t, \alpha_n) : \alpha_n \in \mathcal{M}\}$, and similarly correlates the received quadrature signal over one symbol interval with *all possible* transmitted quadrature alternatives over that symbol interval, namely $\{Q(t, \alpha_n) : \alpha_n \in \mathcal{M}\}$.

Substituting for $I(t, \alpha_n)$ and $Q(t, \alpha_n)$ from equations (3) and (4), respectively, and for $\phi(t, \boldsymbol{\alpha}) = \phi(t, \alpha_n)$ from equation (14), and applying a trigonometric identity gives

$$
\begin{aligned}
Z_n(\alpha_n, \theta_n) \quad = \quad & \sqrt{2E_s/T_s} \cos(\theta_n) \int_{nT_s}^{(n+1)T_s} \widetilde{I}(t, \alpha_n) \cos\theta(t, \alpha_n)\, dt \\
& + \sqrt{2E_s/T_s} \cos(\theta_n) \int_{nT_s}^{(n+1)T_s} \widetilde{Q}(t, \alpha_n) \sin\theta(t, \alpha_n)\, dt \\
& + \sqrt{2E_s/T_s} \sin(\theta_n) \int_{nT_s}^{(n+1)T_s} \widetilde{Q}(t, \alpha_n) \cos\theta(t, \alpha_n)\, dt \\
& - \sqrt{2E_s/T_s} \sin(\theta_n) \int_{nT_s}^{(n+1)T_s} \widetilde{I}(t, \alpha_n) \sin\theta(t, \alpha_n)\, dt, \quad (27)
\end{aligned}
$$

which makes explicit the dependence of $Z_n(\alpha_n, \theta_n)$ on both α_n and θ_n. The quantities $\{Z_n(\alpha_n, \theta_n) : \alpha_n \in \mathcal{M}, \theta_n \in \Theta\}$ output by the receiver (Fig. 4) are the *branch metrics* of the Viterbi algorithm (section 2.6.3). Clearly then, there are at most $M|\Theta|$ values of $Z_n(\alpha_n, \theta_n)$ over each symbol interval; in fact, there can be fewer values of $Z_n(\alpha_n, \theta_n)$, such as for constant-h CPM waveforms (Remark 1) or the MIL-STD-188-181B MHCPM waveforms (Example 2) which only have $M|\Theta|/2$ values of $Z_n(\alpha_n, \theta_n)$ over each symbol interval.

2.6   Simulation

In our simulations we assume a baseband transmitter (Fig. 1) and a baseband correlation receiver (Fig. 4) so that our results are independent of carrier frequency, f_0, and bit rate, R_b. For the purposes of simulation, time must be discretized, or sampled, and the equations evaluated at sampled points. This is accomplished by setting a *sampling frequency*, f_{sam}, defined as the number of samples per symbol interval, T_s, and by defining the *sampling interval*, T_{sam}, as $T_{\mathrm{sam}} \triangleq T_s/f_{\mathrm{sam}}$. As implemented in the simulations, the equations from previous sections are evaluated at times $t = nT_s + kT_{\mathrm{sam}}$, where $k = 0, 1, 2, \ldots, f_{\mathrm{sam}} - 1$ and $n = 0, 1, \ldots, I$.

Example 3 *Consider the case when $g(t)$ is the 1REC pulse, so that, according to equation (6), $q(t)$ is a ramp function (Fig. 2, 1REC) given by*

$$q(t) = \begin{cases} 0, & \text{if } t \leq 0 \\ \frac{t}{2T_s}, & \text{if } 0 \leq t \leq T_s \\ \frac{1}{2}, & \text{if } t \geq T_s. \end{cases}$$

Evaluating equation (15) at sampled points $t = nT_s + kT_{sam}$ and substituting into equation (14) gives

$$\begin{aligned} \phi(nT_s + kT_{sam}, \alpha_n) &= 2\pi h \alpha_n q(kT_{sam}) + \theta_n \\ &= (2\pi h \alpha_n)\frac{kT_{sam}}{2T_s} + \theta_n \\ &= \pi h \alpha_n \frac{k}{f_{sam}} + \theta_n, \end{aligned} \tag{28}$$

for $k = 0, 1, 2, \ldots, f_{sam} - 1$ and $n = 0, 1, \ldots, I$. We note that when evaluated at sampled values, ϕ is independent of T_s, and hence of R_b as claimed, and we remind the reader that successive values of θ_n may be obtained from a look-up table as in Example 1 (Table 1).

Simulation of the encoding is accomplished by a program which performs the functions of the Serial-to-Parallel, Binary-to-M-ary Mapping, and M-ary CPM Modulator blocks in the baseband CPM transmitter diagram (Fig. 1), as described below in section 2.6.1. Simulation of the baseband correlation receiver (Fig. 4) is described in section 2.6.2, and finally simulation of the decoding is described in section 2.6.3.

2.6.1 Encoding

Serial-to-Parallel This code groups the incoming stream of bits into successive blocks of information bits.

1. inputs:

   - sequence of randomly generated bits, $b_{i'}$, for $i' = 1, 2, \ldots, I'$
   - value of M (MIL-STD is 4)

2. computations:

   - $m = \log_2 M$

3. outputs:

   - input bits, $b_{i'}$, grouped into sequence of blocks, $\boldsymbol{b}_i$, each containing m bits

Binary-to-M-ary   This code maps each block of m information bits into an M-ary symbol alphabet.

1. inputs:

   - value of M (MIL-STD is 4), which must be representable as a power of 2
   - sequence of blocks, $\boldsymbol{b}_i$, each containing m bits

2. computations:

   - generation of M-ary alphabet, $\mathcal{M} = \{\pm 1, \pm 3, \dots, \pm(M-1)\}$
   - binary-to-M-ary map

3. outputs:

   - value of $\alpha_i \in \mathcal{M}$ corresponding to each input block, $\boldsymbol{b}_i$, for $i = 0, 1, 2, \dots, I$

M-ary CPM Modulator   This code generates samples of the CPM waveform. For simplicity, we restrict our description to the MIL-STD MHCPM waveform, where $H = 2$ and $g(t)$ is the 1REC pulse.

1. inputs:

   - values of M (MIL-STD is 4), $h_{\underline{0}}$, $h_{\underline{1}}$, and f_{sam}
   - values of α_i, for $i = 0, 1, 2, \dots, I$

2. computations:

   - initialize θ_0 to $S_0 = 0$
   - generate phase state look-up table, as in Example 1 (Table 1), for each value of $h_{\underline{i}}$
   - compute values of $\frac{k}{f_{\text{sam}}}$ for $k = 0, 1, 2, \dots, f_{\text{sam}} - 1$
   - compute values of $\phi(t, \boldsymbol{\alpha})$ at sampled points using equation (28), with $h_{\underline{0}}$ or $h_{\underline{1}}$ substituted for h, and with values of θ_n obtained from a look-up table
   - compute values of $I(t, \boldsymbol{\alpha})$ and $Q(t, \boldsymbol{\alpha})$ at sampled points from equations (3) and (4), respectively

3. outputs:

   - values of $I(t, \boldsymbol{\alpha})$ and $Q(t, \boldsymbol{\alpha})$ at sampled points

2.6.2 Baseband Correlation Receiver

For the purposes of simulation the branch metrics, $Z_n(\alpha_n, \theta_n)$, output by the baseband correlator receiver (Fig. 4), are estimated by approximating each of the integrals in equation (27) by *Riemann sums*. For example, the Riemann sum approximation of the integral

$$\int_{nT_s}^{(n+1)T_s} f(t)\,dt$$

based on samples of $f(t)$ at points $t = nT_s + kT_{\mathrm{sam}}$, is given by

$$\sum_{k=0}^{f_{\mathrm{sam}}-1} T_{\mathrm{sam}} f(nT_s + kT_{\mathrm{sam}}).$$

Denoting *samples* of $\widetilde{I}(t, \alpha_n)$ at times $t = nT_s + kT_{\mathrm{sam}}$ by $\widetilde{I}^{(n,k)}(\alpha_n)$ and using equation (25) it follows that

$$
\begin{aligned}
\widetilde{I}^{(n,k)}(\alpha_n) &\triangleq \widetilde{I}(nT_s + kT_{\mathrm{sam}}, \alpha_n) \\
&= \sqrt{2E_s/T_s}\, I^{(n,k)}(\alpha_n) + I_N^{(n,k)},
\end{aligned}
\tag{29}
$$

where

$$I^{(n,k)}(\alpha_n) \triangleq I(nT_s + kT_{\mathrm{sam}}, \alpha_n) \tag{30}$$

and

$$I_N^{(n,k)} \triangleq I_N(nT_s + kT_{\mathrm{sam}}) \tag{31}$$

denote *samples* of $I(t, \alpha_n)$ and $I_N(t)$, respectively. Using the same notation, it follows from equation (26) that *samples* of $\widetilde{Q}(t, \alpha_n)$ are given by

$$
\begin{aligned}
\widetilde{Q}^{(n,k)}(\alpha_n) &\triangleq \widetilde{Q}(nT_s + kT_{\mathrm{sam}}, \alpha_n) \\
&= \sqrt{2E_s/T_s}\, Q^{(n,k)}(\alpha_n) + Q_N^{(n,k)},
\end{aligned}
\tag{32}
$$

where

$$Q^{(n,k)}(\alpha_n) \triangleq Q(nT_s + kT_{\mathrm{sam}}, \alpha_n) \tag{33}$$

and

$$Q_N^{(n,k)} \triangleq Q_N(nT_s + kT_{\mathrm{sam}}) \tag{34}$$

denote *samples* of $Q(t, \alpha_n)$ and $Q_N(t)$, respectively.

From the properties of BPWGN and equation (18), we observe that $I_N(t)$ and $Q_N(t)$ are independent Gaussian processes with identical rectangular spectral density functions given by

$$S_{I_N}(f) = S_{Q_N}(f) = \begin{cases} \mathcal{N}_0, & \text{if } |f| \leq 1/2T_{\mathrm{sam}} \\ 0, & \text{otherwise.} \end{cases}$$

14

Since $I_N^{(n,k)}$ and $Q_N^{(n,k)}$ are samples from $I_N(t)$ and $Q_N(t)$, respectively, taken at the Nyquist rate of $1/T_{\mathrm{sam}}$, it follows that $I_N^{(n,k)}$ and $Q_N^{(n,k)}$ are each sequences of independent, identically distributed, discrete Gaussian random variables with mean 0 and common variance given by $\mathcal{N}_0/T_{\mathrm{sam}} = \mathcal{N}_0 f_{\mathrm{sam}}/T_s$. Therefore, we define new discrete Gaussian random variables, $\mathcal{I}_N^{(n,k)} = \sqrt{T_s} I_N^{(n,k)}$ and $\mathcal{Q}_N^{(n,k)} = \sqrt{T_s} Q_N^{(n,k)}$, having mean 0 and common variance given by $\mathcal{N}_0 f_{\mathrm{sam}}$, which is independent of T_s and hence of R_b.

From equation (15) we see that sampling the functions $\cos\theta(t,\alpha_n)$ and $\sin\theta(t,\alpha_n)$ at times $t = nT_s + kT_{\mathrm{sam}}$ gives

$$\cos\theta(nT_s + kT_{\mathrm{sam}}, \alpha_n) = \cos[2\pi h_{\underline{n}}\alpha_n q(kT_{\mathrm{sam}})] \tag{35}$$

and

$$\sin\theta(nT_s + kT_{\mathrm{sam}}, \alpha_n) = \sin[2\pi h_{\underline{n}}\alpha_n q(kT_{\mathrm{sam}})]. \tag{36}$$

Finally, substituting $\mathcal{I}_N^{(n,k)}/\sqrt{T_s}$ for $I_N^{(n,k)}$ in equation (29) and $\mathcal{Q}_N^{(n,k)}/\sqrt{T_s}$ for $Q_N^{(n,k)}$ in equation (32) and using equations (35) and (36), the *discrete Riemann sum approximation* of the branch metrics, $Z_n(\alpha_n, \theta_n)$ defined above in equation (27), is given by

$$
\begin{aligned}
Z_n^{(\mathrm{dis})}(\alpha_n, \theta_n) \;=\; & \frac{\sqrt{2E_s}}{f_{\mathrm{sam}}}\cos(\theta_n)\sum_{k=0}^{f_{\mathrm{sam}}-1}(\sqrt{2E_s}I^{(n,k)}(\alpha_n) + \mathcal{I}_N^{(n,k)})\cos[2\pi h_{\underline{n}}\alpha_n q(kT_{\mathrm{sam}})] \\
& + \frac{\sqrt{2E_s}}{f_{\mathrm{sam}}}\cos(\theta_n)\sum_{k=0}^{f_{\mathrm{sam}}-1}(\sqrt{2E_s}Q^{(n,k)}(\alpha_n) + \mathcal{Q}_N^{(n,k)})\sin[2\pi h_{\underline{n}}\alpha_n q(kT_{\mathrm{sam}})] \\
& + \frac{\sqrt{2E_s}}{f_{\mathrm{sam}}}\sin(\theta_n)\sum_{k=0}^{f_{\mathrm{sam}}-1}(\sqrt{2E_s}Q^{(n,k)}(\alpha_n) + \mathcal{Q}_N^{(n,k)})\cos[2\pi h_{\underline{n}}\alpha_n q(kT_{\mathrm{sam}})] \\
& - \frac{\sqrt{2E_s}}{f_{\mathrm{sam}}}\sin(\theta_n)\sum_{k=0}^{f_{\mathrm{sam}}-1}(\sqrt{2E_s}I^{(n,k)}(\alpha_n) + \mathcal{I}_N^{(n,k)})\sin[2\pi h_{\underline{n}}\alpha_n q(kT_{\mathrm{sam}})],
\end{aligned}
$$

for $n = 0, 1, \ldots, I-1$. For the case when $g(t)$ is the 1REC pulse, the arguments in the cosine and sine terms in the above equation simplify further as in equation (28) to $\pi h_{\underline{n}}\alpha_n k/f_{\mathrm{sam}}$. In the 1REC case, then, it is clear that $Z_n^{(\mathrm{dis})}(\alpha_n, \theta_n)$ is independent of f_0 and R_b as claimed for our simulations.

2.6.3 Decoding

Since we consider only practical CPM systems which are representable as finite-state systems with an associated trellis (section 2.3), decoding is possible using the Viterbi algorithm (VA) in much the same way as the VA is used for decoding convolutional codes. The VA is a recursive procedure to obtain an optimal solution to the estimation of the state sequence of a finite-state Markov process observed in memoryless noise [7]. The VA is optimum in the sense of providing

a maximum likelihood estimate of the sequence of states, called a maximum likelihood sequence estimate (MLSE). Since a specific sequence of state transitions arises from a unique sequence of data symbols, a MLSE of states is also a MLSE of the data symbols, α_i, and hence, of the message bits, $b_{i'}$.

3 Coded CPM Waveform

CPM by itself may be viewed as a coding operation, since the phase process exhibits memory in the state vector as described above in section 2.3. Coded CPM is obtained by precoding the digital symbol inputs to the modulator as detailed below.

3.1 Waveform Definition

The precoding of the digital symbol inputs required in coded CPM is accomplished by inserting a forward error correction (FEC) encoder with rate $R_c = l/m$ between the Serial to Parallel and the Binary to M-ary Mapping blocks in the baseband CPM transmitter block diagram (Fig. 1) as seen below (Fig. 5). Thus, the *symbol rate* for coded CPM is given by $R_s = \frac{R_b/R_c}{m} = \frac{R_b}{mR_c}$, compared to R_b/m for uncoded CPM (section 2.1).
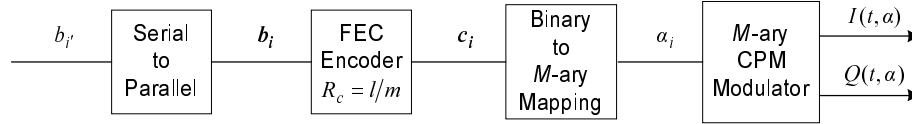

Figure 5: Block diagram of coded CPM transmitter.

In this paper the FEC encoder is either a *linear block* code or a *non-recursive convolutional* code; therefore, any references below to convolutional codes should be understood to mean non-recursive. As in Proakis [8, section 8-2] we assume that the convolutional code is of constraint length, K, comprising K consecutive shift registers, each containing l bits, allowing for the input information bits to be shifted into and along the sequence of shift registers l bits at a time.

For each of the two types of encoder considered here, l information bits, denoted by $\boldsymbol{b}_i = (b_{il}, b_{il+1}, \ldots, b_{il+(l-1)})$, are input, producing m output code bits, denoted by $\boldsymbol{c}_i = (c_{im}, c_{im+1}, \ldots, c_{im+(m-1)})$, where $i = \ldots, -1, 0, +1, \ldots$. Linear block encoders are said to be *memoryless* since the coded bits, $\boldsymbol{c}_i$, depend only on $\boldsymbol{b}_i$ as determined by m linear functions of the l bits contained in $\boldsymbol{b}_i$; in practice the linear functions are usually represented by m column vectors in an $l \times m$ generator matrix. By contrast, convolutional encoders are said to have a *memory* since the coded bits, $\boldsymbol{c}_i$, depend not only on $\boldsymbol{b}_i$ but also on the $(K-1)l$ preceding bits as determined by m linear functions of the Kl bits contained in $\boldsymbol{b}_i, \boldsymbol{b}_{i-1}, \boldsymbol{b}_{i-2}, \ldots, \boldsymbol{b}_{i-(K-1)}$. (For convolutional codes it is assumed that $K > 1$,

since the case that $K = 1$ reduces to a linear block code.) As in Pizzi and Wilson [9] we describe the encoding operation for either linear block codes or convolutional codes and the subsequent mapping operation functionally as

$$\alpha_i = f(\boldsymbol{b}_i, \boldsymbol{b}_{i-1}, \ldots, \boldsymbol{b}_{i-(K-1)}),\tag{37}$$

where $K = 1$ for linear block codes or $K > 1$ for convolutional codes.

3.2   Performance Trade-Offs

Coded CPM offers the benefit of potential coding gain at the cost of bandwidth expansion attributable to the code redundancy and increased complexity attributable to the longer memory, as will be seen in the next section. Using the 99% power in band definition of bandwidth, Anderson *et al.* [2, section 11.3.4] estimates that the bandwidth of a rate-R_c coded CPM waveform is greater than the bandwidth of an uncoded CPM waveform by the factor $1/R_c$. Also, while the number of states in uncoded CPM is given by $pM^{(L-1)}$, as seen from equation (13), the number of states in coded CPM increases exponentially to $pM^{(L-1)+(K-1)}$, as will be seen from equation (39) in the next section.

Anderson *et al.* [2, section 11.3.5] remark that good coded CPFSK schemes have been found by employing a high rate convolutional code, a large symbol alphabet, $\mathcal{M}$, and a low modulation index. They remark further that by varying the system parameters, particularly the modulation index, different combinations of bandwidth and power savings can be achieved.

3.3   State Model

Given the definition of the state vector, $\boldsymbol{\sigma}_n$, in section 2.3 and the functional dependence of equation (37), it follows that for linear block or convolutionally encoded CPM the state vector could be defined in terms of the input data as

$$\boldsymbol{\sigma}_n = (\theta_n, \boldsymbol{b}_{n-1}, \boldsymbol{b}_{n-2}, \ldots, \boldsymbol{b}_{n-(L-1)-(K-1)}),\tag{38}$$

which demonstrates the combined effects of pulse length, L, and coding on memory. Note that when $l = 1$ the state vector for encoded CPM simplifies to

$$\boldsymbol{\sigma}_n = (\theta_n, b_{n-1}, b_{n-2}, \ldots, b_{n-(L-1)-(K-1)}),\tag{39}$$

which has the same form as equation (38) but reveals a dependence on the individual information bits.

4   Synchronization Methods

For coherent detection, knowledge of the carrier frequency and phase and of the data symbol transition instants must be available to the receiver. The process of determining these parameters is known as *synchronization*. We employed the synchronization method developed by Miller, Harris, and Stephens [10] for

the MHCPM waveform which was adopted by MIL-STD-188-181B [1]. In this method, synchronization is achieved at the receiver by processing a *preamble*, transmitted as an MSK (binary) signal at the 4-ary data symbol rate and immediately preceding the data transmission (Fig. 6). The preamble contains three fields: a Preamble Bit Pattern (PBP) followed by a Start of Message (SOM) marker, both of which are used for synchronization, and then a Header containing modulation, forward error correction and interleaver information pertaining to the transmitted data.

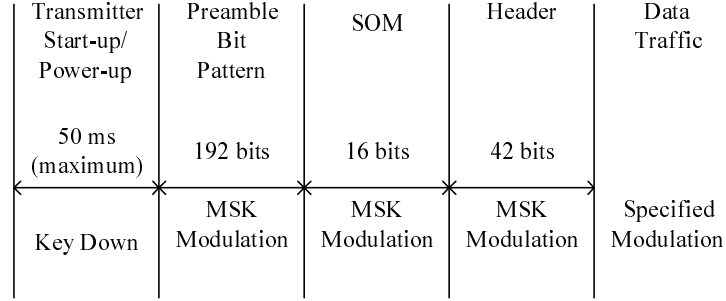| Transmitter Start-up/ Power-up	Preamble Bit Pattern	SOM	Header	Data Traffic
50 ms (maximum)	192 bits	16 bits	42 bits	
Key Down	MSK Modulation	MSK Modulation	MSK Modulation	Specified Modulation

Figure 6: Synchronization method for MHCPM.

The PBP is a 192-bit string, comprising 48 consecutive repetitions of the 4-bit sequence, 1100, and has a power spectrum with tones centered at $f_0 + n f_{sym}/4$, where f_{sym} is the symbol rate that will be used during the data transmission and n is any integer. Only terms corresponding to $n = 0, \pm 1$, and ± 2, however, have significant energy. *Carrier frequency, carrier phase, timing information,* and *symbol rate* are estimated from the features of a fast Fourier transform (FFT) of the PBP. Specifically, carrier frequency is estimated by the frequency of the $n = 0$ tone, carrier phase is estimated by the phase of the $n = 0$ tone, symbol phase (timing) is estimated from the phase of the tones at $n = \pm 1$ and at $n = 0$, and symbol rate is estimated from the spacing between the $n = 0$ and $n = \pm 1$ tones. Finally, timing of the modulation indices, called *superbaud timing,* and timing required for demand assigned multiple access (DAMA) schemes, called *frame synchronization*, are established from the output of a correlator operating on the 16-bit SOM sequence, 1010 1100 0011 1011.

5 Simulation Results

We conducted two simulation studies, first of performance results for uncoded and coded MHCPM assuming perfect synchronization (section 5.1) and then performance results in acquiring synchronization (section 5.2) using the methods of section 4.

5.1 Assuming Synchronization

We performed simulations of 4-ary ($M = 4$) MHCPM with a full-response ($L = 1$) rectangular frequency pulse (1REC) using the five sets of values for $\mathcal{H} = \{h_{\underline{0}}, h_{\underline{1}}\}$ specified in MIL-STD-188-181B [1] and assuming an additive white Gaussian noise channel. We have included plots of our simulation results only for the lowest and highest sets of values of $\mathcal{H}$, $\{4/16, 5/16\}$-CPM (Fig. 7, top) and $\{12/16, 13/16\}$-CPM (Fig. 7, bottom), respectively, since results for the other three sets of values of $\mathcal{H}$ vary between these extremes.

In addition to performance curves for simulation results each plot includes, for comparison, theoretical performance curves for $\{4/16, 5/16\}$-CPM or $\{12/16, 13/16\}$-CPM and for MSK, which is in fact binary ($M = 2$) CPM with a full-response ($L = 1$) rectangular frequency pulse (1REC) and single modulation index $h = 1/2$. The theoretical performance curve for MSK is valid at all values of E_b/N_0 and is identical to the curve for BPSK. The theoretical performance curves for the $\{4/16, 5/16\}$- and $\{12/16, 13/16\}$-CPM waveforms were generated from an approximation based on the minimum distance properties of each CPM waveform given in Anderson *et al.* [2, equation 3.31]. The theoretical CPM waveform curves are valid at high values of E_b/N_0 and provide an estimate of the maximum gain attainable by CPM relative to MSK which, as seen in the plots, is approximately 2.4 dB for the $\{4/16, 5/16\}$-CPM waveform and 4.6 dB for the $\{12/16, 13/16\}$-CPM waveform. The gain of MHCPM relative to MSK is attributable to the increase in H from 1 for MSK to 2 for MHCPM and to the increase in M from 2 for MSK to 4 for MHCPM.

The codes used in the convolutionally encoded CPM simulations were $R_c = 1/2$ and $K = 7$ convolutional codes; whereas the codes used in the Reed-Solomon (RS) encoded CPM simulations were $(60, 50)$ RS codes, shortened from a $(63, 53)$ RS code employing 6-bit code symbols. For our simulations we tried interleavers of depth 4, 8, and 16 symbols with RS codes; however, we included results only from the interleaver of depth 4 symbols since the additional gain with a depth of 8 and 16 symbols was marginal.

Note that above some value of E_b/N_0 in each plot the performance curve for simulated CPM lies between the theoretical performance curves for CPM and MSK as expected. Also note that in the progression from $\{4/16, 5/16\}$-CPM to convolutionally encoded $\{4/16, 5/16\}$-CPM, to RS encoded $\{4/16, 5/16\}$-CPM, and finally to interleaved RS encoded $\{4/16, 5/16\}$-CPM simulated gains relative to MSK at bit error rate 10^{-6} increase monotonically from approximately 1.5 dB to 5 dB (Fig. 7, top). A similar progression of even larger gains is evident in the case of $\{12/16, 13/16\}$-CPM (Fig. 7, bottom) at the cost of greater spectral occupancy than for $\{4/16, 5/16\}$-CPM.

5.2 Acquiring Synchronization

In this simulation we generated a received intermediate frequency 4-ary ($M = 4$) MHCPM waveform corrupted by additive Gaussian noise, and then extracted estimates of the four parameters from features of the FFT of the PBP as described
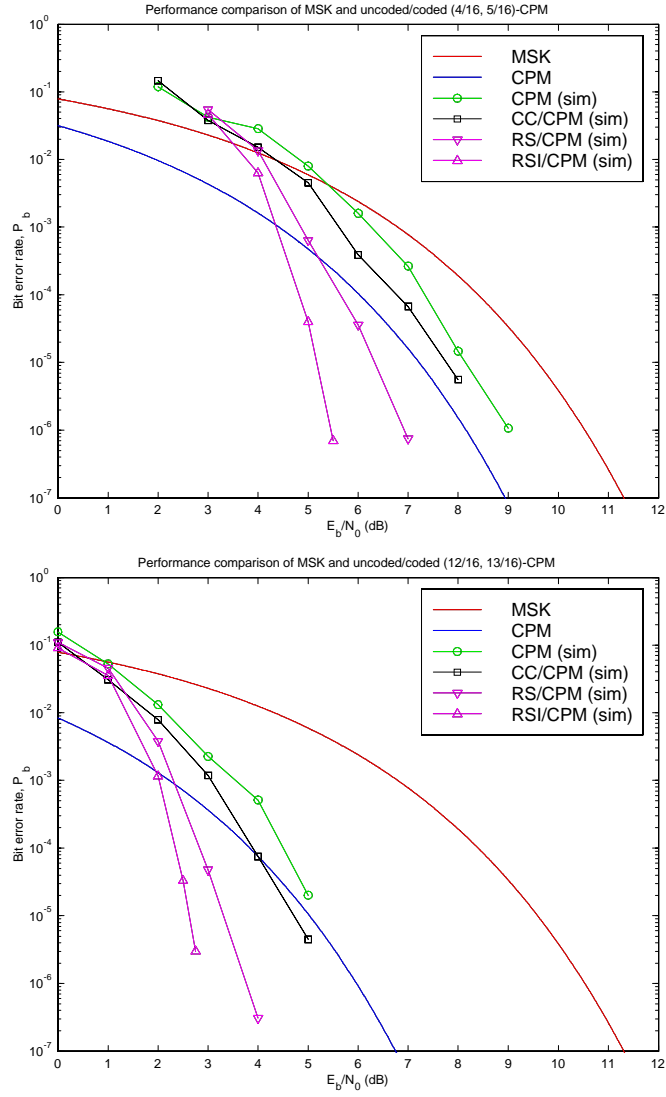
Figure 7: Performance results for theoretical MSK (MSK) and theoretical CPM (CPM) compared to simulated results for CPM (CPM (sim)), convolutionally encoded CPM (CC/CPM (sim)), Reed-Solomon encoded CPM (RS/CPM (sim)), and interleaved Reed-Solomon encoded CPM (RSI/CPM (sim)).

above (section 4). Using these estimated parameters, MSK demodulation and then low-pass filtering was applied to the waveform, followed by MSK decoding using a 1-h CPM decoder. Finally, the known 16-bit SOM sequence was correlated with successive 16-bit strings of the decoded preamble, *i.e.*, with bits $1, 2, \ldots, 16$ ($k = 1$), bits $2, 3, \ldots, 17$ ($k = 2$), $\ldots$, and bits $193, 194, \ldots, 208$ ($k = 193$). For our purposes, synchronization was defined as SOM synchronization, which was achieved when a peak correlation value was obtained for $k = 193$. As seen below (Fig. 8) our estimates of the probability of SOM synchronization obtained from simulation ranged from 0.8966 at -2.0 dB to 0.9996 at 2.0 dB. We observed that unsuccessful, or false acquisition, generally occurred when there were decoding errors in the received SOM sequence.
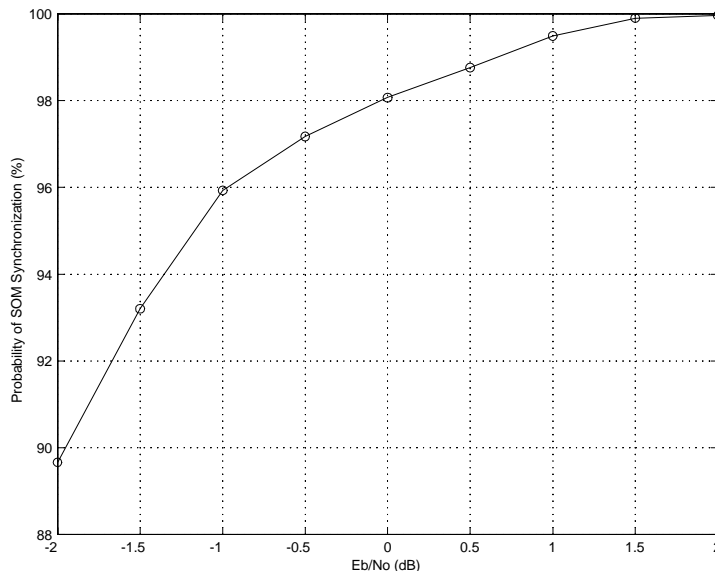

Figure 8: Probability of SOM synchronization for MIL-STD-188-181B.

References

[1] Department of Defense, "Interoperability standard for single-access 5-kHz and 25-kHz UHF satellite communications channels," MIL-STD-188-181B, 20 March 1999.

[2] J. B. Anderson, T. Aulin, and C.-E. Sundberg, *Digital Phase Modulation*, New York: Plenum Press, 1986.

[3] T. Aulin and C.-E. W. Sundberg, "Continuous phase modulation–Part I: full response signaling," *IEEE Transactions on Communications*, vol. COM-29, no. 3, pp. 196–209, Mar. 1981.

[4] T. Aulin, N. Rydbeck, and C.-E. W. Sundberg, "Continuous phase modulation–Part II: partial response signaling," *IEEE Transactions on Communications*, vol. COM-29, no. 3, pp. 210–225, Mar. 1981.

[5] I. Sasase and S. Mori, "Multi-h Phase-Coded Modulation," *IEEE Communications Magazine*, vol. 29, no. 12, pp. 46–56, Dec. 1991.

[6] J. B. Anderson and C.-E. W. Sundberg, "Overview of advances in constant-envelope coded modulation," in *Coded Modulation and Bandwidth-Efficient Transmission: Proceedings of the Fifth Tirrenia International Workshop on Digital Communications*, pp. 15–26, 1992.

[7] G. D. Forney, Jr., "The Viterbi algorithm," *Proceedings of the IEEE*, vol. 61, no. 3, pp. 268–278, Mar. 1973.

[8] J. G. Proakis, *Digital Communications*, Third Edition, New York: McGraw-Hill, 1995.

[9] S. V. Pizzi and S. G. Wilson, "Convolutional coding combined with continuous phase modulation," *IEEE Transactions on Communications*, vol. COM-33, no. 1, pp. 20–29, Jan. 1985.

[10] M. Miller, M. Harris, and D. R. Stephens, "An innovative synchronization preamble for UHF MILSATCOM," *Proceedings of MILCOM '99.*